Thermal Stability of an Mg–Nd Alloy Processed by High-Pressure Torsion

Samia Tighiouaret, Rabeb Lachhab, Abdelkader Hanna, Hiba Azzeddine, Yi Huang, Thierry Baudin, Anne-Laure Helbert, François Brisset, Djamel Bradai, Terence G Langdon

Thermal stability of an Mg-Nd alloy processed by high-pressure torsion

Samia Tighiouaret, Rabeb Lachhab, Abdelkader Hanna, Hiba Azzeddine[*], *Yi Huang, Thierry Baudin, Anne-Laure Helbert, François Brisset, Djamel Bradai, Terence G. Langdon*

Samia Tighiouaret, Dr. Hiba Azzeddine, Abldekader Hanna
Department of Physics,
University of Mohamed Boudiaf
M'sila, 28000, Algeria
E-mail: hiba.azzeddine@univ-msila.dz

Dr. Rabeb Lachhab
Laboratoire de Chimie Inorganique Ur-11-Es-73,
Faculté des Sciences de Sfax
BP 1171, 3018, Sfax Tunisia

Dr. Yi Huang
Department of Design and Engineering
Faculty of Science and Technology,
Bournemouth University,
Poole, Dorset BH12 5BB, UK
Also with
Materials Research Group, Department of Mechanical Engineering
University of Southampton
Southampton SO17 1BJ, UK

Dr. Thierry Baudin
ICMMO, Univ. Paris-Sud
Université Paris-Saclay, UMR CNRS 8182
91405 Orsay Cedex, France

Dr. Anne-Laure Helbert
ICMMO, Univ. Paris-Sud
Université Paris-Saclay, UMR CNRS 8182
91405 Orsay Cedex, France

François Brisset
ICMMO, Univ. Paris-Sud
Université Paris-Saclay, UMR CNRS 8182
91405 Orsay Cedex, France

Prof. Djamel Bradai
Faculty of Physics
University of Sciences and Technology Houari Boumediene
BP 32 El-Alia, 16111, Algiers, Algeria.

Prof. Terence G. Langdon
Materials Research Group, Department of Mechanical Engineering
University of Southampton
Southampton SO17 1BJ, UK

Keywords: high-pressure torsion, Mg-RE alloy, microstructure, recrystallization, texture

The evolution of microstructure, texture and mechanical properties of an Mg-1.43Nd (wt.%) alloy are investigated after processing by high-pressure torsion at room temperature through 5 turns and isochronal annealing for 1 h at 150, 250, 350 and 450 °C using Electron BackScatter Diffraction and Vickers microhardness. The alloy exhibits a good thermal stability up to an annealing at 250 °C, with mean grain size of ~0.65 μm. The microhardness shows an initial hardening after annealing at 150 °C and then a subsequent softening. The deformation texture, a basal texture shifted 60° away from the shear direction (SD), is retained during annealing up to 250 °C. By contrast, a basal texture with symmetrical splitting towards SD is developed after annealing at 350 °C. The precipitation sequence and their pinning effect are responsible for the age-hardening, stabilization of grain size and the texture modification. The kinetics of grain growth in the Mg-1.43Nd alloy follows two stages depending on the temperature annealing range, with an activation energy of ~26 kJ/mol in the low temperature range of 150–250 °C and ~147 kJ/mol in the high temperature range of 250–450 °C.

1. Introduction

Over the last decade magnesium-rare earth (Mg-RE) alloys have been widely investigated with the objective of replacing the conventional Mg-based alloy such as AZ31 (Mg-3Al-1Zn, wt.%) in numerous industrial applications. [1, 2] In practice, the presence of RE elements in dilute binary Mg-RE alloys, or even as additional alloying elements in ternary Mg-based alloys, have proven their efficiency in improving the room temperature formability and enhancing the strength and creep resistance through the development of a weak texture that is different from the typical basal texture. [1–3] For example, deformation by extrusion of Mg-RE alloys leads to the development of a new texture designated “rare earth texture” where the $[2\bar{1}\bar{1}1]$ of grains is parallel to the extrusion direction (ED). [4, 5] By contrast, a texture named

“TD-split texture”, where the basal (0002) poles of the grains are tilted from the normal direction (ND) towards the transverse direction (TD), was reported in hot-rolled Mg-RE alloys. [6, 7]

It is recognized that recrystallization and grain growth processes are responsible for the weak and unusual textures in Mg-RE alloys. [1] Hence, many theories have been established in attempts to explain the mechanisms responsible for the special effect of RE elements on texture modification. First, it was attributed to a particle-stimulated nucleation (PSN) mechanism after processing. [8] Then the nucleation and growth of new oriented grains was highlighted at deformation features such as shear bands [9] or twins. [10] Also, it was proposed that the activation of non-basal slip systems and the changing of grain boundary mobilities by solute drag may also affect the final texture. [11, 12]

Another positive effect of RE elements on Mg-based alloys is the additional ductility provided by grain refinement [13] which ensures a high thermal stability of the refined microstructure during annealing due to a solute-grain boundary drag at lower annealing temperatures. For example, the low diffusivity (~10^{-22} m^2/s) of Nd in Mg at 177 °C [14] and the precipitation of different metastable and stable phases during annealing which retard the grain boundary mobility. [15–17]

Nevertheless, it is necessary in practice to increase the performance of Mg-RE alloys in order to extend their use in the automotive and aerospace industries or for use in biomedical applications. Severe plastic deformation (SPD) by equal-channel angular pressing (ECAP) or high-pressure torsion (HPT) appears to be an excellent strategy for improving the mechanical and superplastic properties of Mg-based alloys through the production of excellent grain refinement, down to the sub-micrometer level, and by introducing a high density of defects. [18–21]

Moreover, Mg-RE alloys have proven their efficiency in producing very significant grain refinement compared to conventional Mg-based alloy after SPD processing. [22–25] For

example, the Mg-10Gd (wt.%) alloy exhibits an average grain size of ~100 nm against ~1 μm in the AZ31 alloy after similar HPT processing. [22, 23]

Several studies were conducted earlier on the binary Mg-RE processed by HPT in an attempt to extend the fundamental understanding of the effect of RE elements and SPD processing on the precipitation, recrystallization and gain growth phenomena. [26–30] First, the effect of HPT processing on the microstructural and textural evolution in Mg-1.43Nd, Mg-1.44Ce and Mg-1.44Dy (%.wt) alloys was investigated. [28, 29] Second, the sequence and kinetics of pre-precipitation in a Mg-1.43Nd alloy was investigated after HPT processing using *in situ* synchrotron X-ray diffraction and differential scanning calorimetry (DSC). [27] Third, the recrystallization process and thermal stability after HPT processing was characterized by DSC and EBSD in Mg-1.44Ce and Mg-1.44Dy alloys, respectively. [26, 30] However, the thermal stability of Mg-1.44Dy was investigated at only two annealing temperatures (200 and 400 °C for 1 h). [30] Thus, the main objective of the present study was to extend an investigation of the thermal stability of an HPT-processed Mg-RE alloys over a large range of annealing temperatures in order to attain a more comprehensive analysis of the recrystallization and grain growth phenomena of Mg-RE alloys. Accordingly, the evolution of microstructure, texture and mechanical properties of the Mg-1.43Nd alloy were investigated after HPT processing at room temperature through 5 turns and isochronal annealing for 1 h at temperatures of 150, 250, 350 and 450 °C using electron backscatter diffraction (EBSD) and Vickers microhardness. The grain growth kinetics of the alloy were also investigated during the isochronal annealing.

2. Materials and Methods

An as-cast Mg-1.43Nd (wt.%) alloy was supplied from the Institut für Metallkunde und Metallphysik (IMM-RWTH) in Aachen, Germany. The alloy was produced by induction

melting and casting under a protective gas atmosphere of Ar/CO_2 followed by a heat treatment for 20 h at 420 °C.

The HPT processing was conducted on discs with diameters of 10 mm and thicknesses of 0.9 mm at room temperature through 5 turns using an imposed applied pressure of 6.0 GPa and with a rotational speed of 1 rpm under quasi-constrained conditions. [31] Processing through 5 turns was selected based on an earlier investigation demonstrating that these conditions produce homogeneous ultra-fine grains in Mg-RE alloys. [29] After the processing by HPT, annealing was carried out at temperatures of 150, 250, 350 or 450 °C for 1 h in a radiation furnace followed by quenching in water.

The microstructures of the processed and annealed samples were investigated near the centres of the discs using electron backscatter diffraction (EBSD) in the RD-SD plane after mechanical and ionic polishing using a Gatan PECS II system at a high voltage of 5 kV for 15 min, where RD and SD denote the rotational and shear directions, respectively. The observations were carried out using a scanning electron microscope FEG-SEM SUPRA 55 VP operating at 20 kV. The scanned areas were 50 × 50 μm^2 with a 50 nm step size for samples annealed at 150, 250 and 350 °C and 300 × 300 μm^2 with a 0.5 μm step size for sample annealed at 450 °C. The EBSD data acquisition and analysis were undertaken using the TSL Orientation Imaging Microscopy, OIM^{TM} software. The grain size data were obtained using a grain tolerance angle of 5° and the minimum grain size was chosen as 5 pixels. All datum points with a confidence index (CI) lower than 0.05 were excluded from the analysis, where the CI quantifies the reliability of the indexed pattern.

Quantitative texture analysis was carried out by calculating the Orientation Distribution Function (ODF) using the MTex software. [32] The ODF was calculated using the harmonic method (L = 22) with each orientation modeled with a Gaussian function having a half-width of 5°.

The Vickers microhardness was measured at the centre of the discs using a SHIMADZU type HMV-2 tester. An average microhardness value was obtained using at least three indentations under a load of 100 g ($Hv_{0.1}$) with a dwell time of 10 s.

3. Results

3.1 .Microstructural evolution

The microstructures in terms of the orientation imaging micrographs in the inverse pole figure (IPF) maps of the HPT-processed and the annealed Mg-1.43Nd alloy after 1 h at 150, 250, 350 and 450 °C are illustrated in Figure 1.

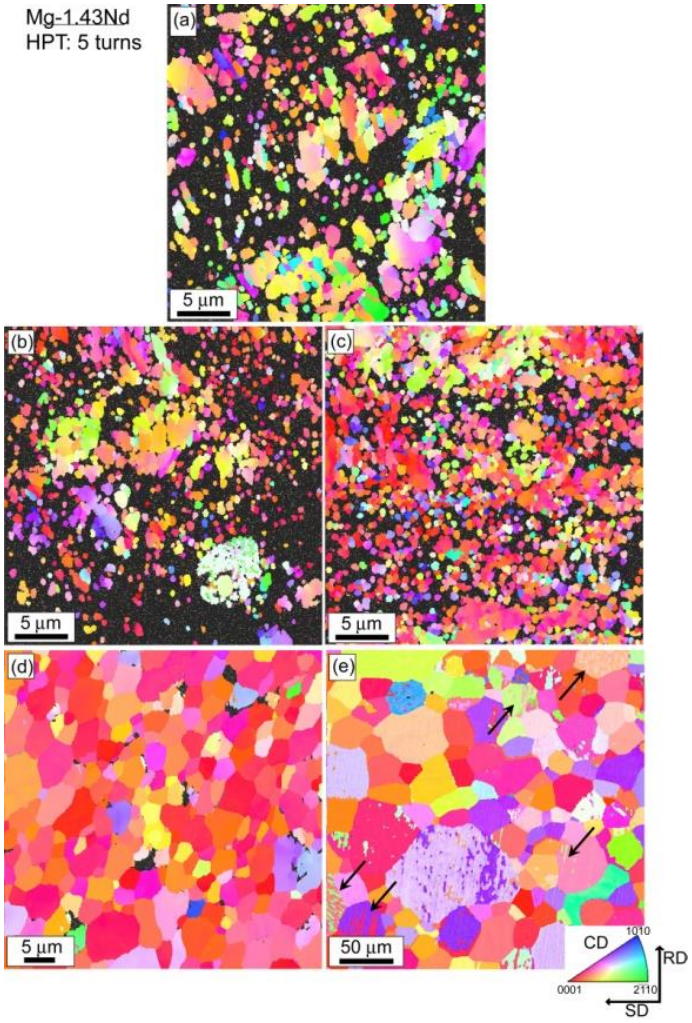

Figure 1: Inverse pole figure maps of Mg-1.43Nd alloy after (a) 5 HPT turns and subsequent annealing for 1 h at: (b) 150 °C, (c) 250 °C, (d) 350 °C and (e) 450 °C.

The black zones present in the microstructures of the 5 HPT turns sample and after annealing at 150 °C and 250 °C indicate highly deformed areas of the samples. As expected, the areas of black zones decrease with increasing annealing temperature because of the increase in recrystallized grains and the consequent decrease in the microstructural heterogeneities. Annealing starting from 350 °C appears to produce a complete recrystallization with a homogenous microstructure of equiaxed grains. Annealing twins are visible in the sample annealed at 450 °C, indicated by arrows in Figure 1(e), and these were determined as tensile twinning (86°/<$2\bar{1}\bar{1}0$>).

Figure 2 shows the evolution of the mean grain size of the Mg-1.43Nd alloy processed by HPT through 5 turns as a function of the annealing temperature. At least two EBSD maps of each sample were used in order to achieve reasonable statistics in estimating the mean grain sizes.

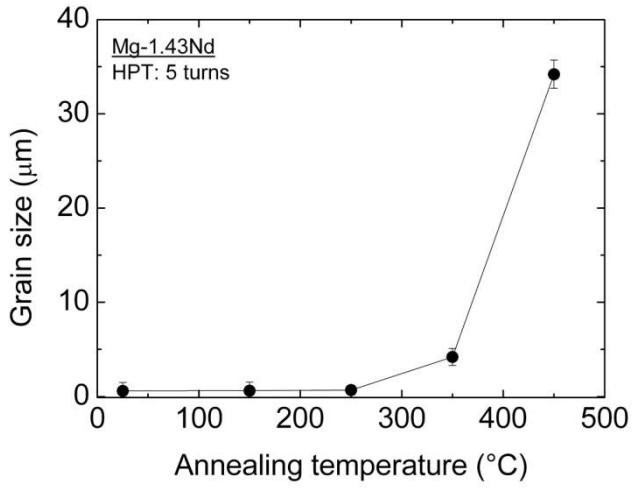

Figure 2: Evolution of mean grain size of Mg-1.43Nd alloy processed by HPT through 5 turns as function of annealing temperature.

It is important to note that the as-cast microstructure exhibited very coarse grains with an average grain size of ~600 μm and HPT processing through 5 turns produced very strong grain refinement with an average grain size of ~0.6 μm. The mean grain size remains stable in annealing at 250 °C but then increases slowly to ~4.2 μm after annealing at 350 °C and

thereafter rapidly increases to ~34 μm after annealing at 450 °C as revealed also in Figure 1(e).

Figure 3 presents the scanning electron microscopy (SEM) micrographs in backscattering mode of the Mg-1.43Nd alloy after 5 HPT turns and subsequent annealing for 1 h at 150, 250, 350 and 450 °C, respectively. It is apparent that all microstructures reveal the presence of second phase particles with diameters in the range of ~1.5–4.5 μm.

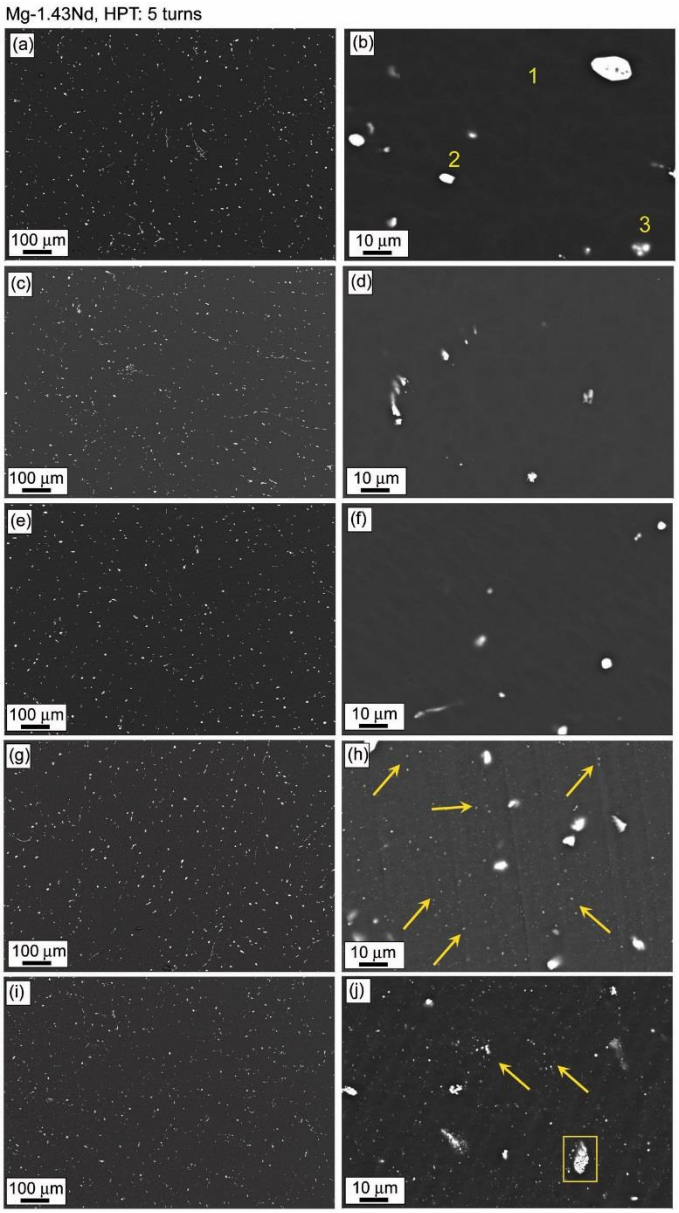

Figure 3: Micrographs by scanning electron microscopy in backscattering mode of the Mg-1.43Nd alloy after (a, b) 5 HPT turns and subsequent annealing for 1 h at: (c, d) 150 °C, (e, f) 250 °C, (g, h) 350 °C and (i, j) 450 °C.

Moreover, the microstructures of samples annealed at 350 and 450 °C are characterized by the presence of well-dispersed fine particles with spherical shapes as shown by the arrows. Unfortunately, precise identifications of the chemical compositions of these particles was not easy using energy-dispersive X-ray spectroscopy (EDS) analysis because of their very small size of <0.3 μm. Nevertheless, the volume fraction of these second phase particles was calculated by quantitative metallography as ~1.2 ± 0.3% in the deformed samples. Furthermore, their fractions were stable during annealing up to 250 °C and then increased to ~2.9 ± 0.4% after annealing at 450 °C. Table 1 shows the EDS results summarizing the relative proportions of the Mg and Nd elements (in wt.%) in different positions (points 1–3) on the deformed sample in Figure 3(b). Thus, the Mg matrix contains ~1.38% of the Nd element which is close to the anticipated concentration in the Mg-1.43Nd alloy. The particle in point 2 is probably $Mg_{41}Nd_5$ and for point 3 it appears to be the $Mg_{12}Nd$ phase. The presence of $Mg_{12}Nd$ particles is a direct consequence of the slow solidification rate during casting. [33]

Table 1. EDS analysis in weight percentage in different positions in the microstructure of Mg-1.43Nd alloy processed by HPT through 5 turns (shown in Figure 3b).

Element	point 1	point 2	point 3
MgK	98.62	58.14	65.36
NdL	1.38	41.86	34.64

3.2. Texture evolution

Figure 4 shows the recalculated pole figure (0002) for the Mg-1.43Nd alloy after 5 HPT turns and subsequent annealing at temperatures up to 450 °C for 1 h. Thus, HPT processing leads to the development of a basal texture inclined by 60° from RD towards SD, as shown in Figure 4(a). Such deviation from a typical basal texture may be a consequence of a dynamic shearing effect during the HPT processing. The textures after annealing at 150 and

250 °C are very similar to the deformed texture. However, the low texture intensity observed in the sample annealed at 150 °C is related to the small number of grains taken from the EBSD map in Figure 1(b) compared to the other EBSD maps. By contrast, a typical basal texture develops starting from annealing at 350 °C with symmetrical splitting towards the SD. The texture intensity remains stable after annealing at 450 °C (~6.2 mrd corresponding to multiples of a random distribution) but the distribution of the (0002) poles are less symmetrical and more spread away from the SD.

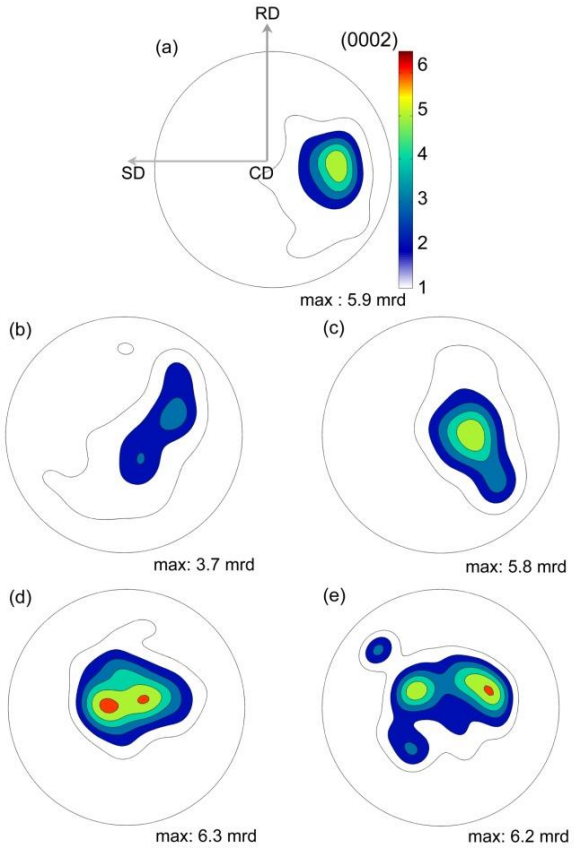

Figure 4: Recalculated basal (0002) pole figures of the Mg-1.43Nd alloy after (a) 5 HPT turns and subsequent annealing for 1 h at: (b) 150 °C, (c) 250 °C, (d) 350 °C and (e) 450 °C.

3.3. Microhardness evolution

Figure 5 shows the evolution of the microhardness of the Mg-1.43Nd alloy processed by HPT through 5 turns as a function of the annealing temperature up to 450 °C. First, the microhardness increases from 79 ± 3 Hv after 5 HPT turns to 98 ± 3 Hv after annealing at

150 °C thereby causing a hardening. Second, the microhardness then decreases with increasing annealing temperature to reach a value of 47 ± 4 Hv after annealing at 450 °C which is similar to the microhardness of the as-cast alloy at 44 ± 3 Hv.

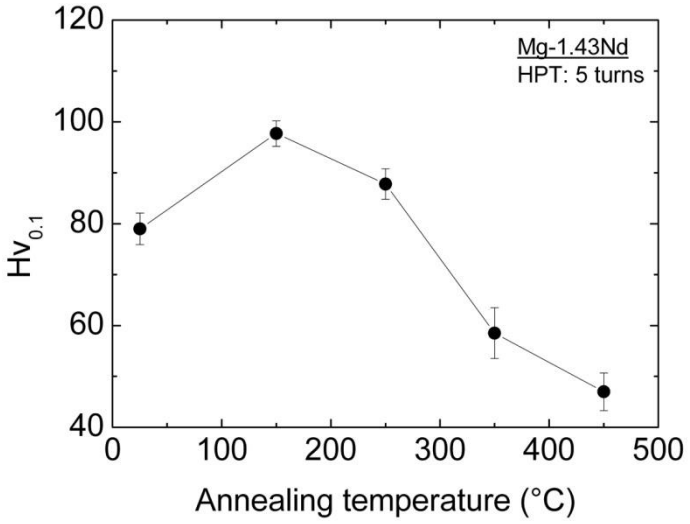

Figure 5: Evolution of the microhardness of Mg-1.43Nd alloy processed by HPT through 5 turns as function of annealing temperature.

4. Discussion

The present investigation deals with the evolution of microstructure, texture and mechanical properties in an HPT-processed Mg-1.43Nd alloy during isochronal annealing. As shown in Figs 1 and 3, the alloy exhibits a good thermal stability when annealing at 250 °C. However, the evolution of microhardness as a function of annealing temperature shows an initial hardening after annealing at 150 °C and then a subsequent softening. In practice, the precipitation sequence is responsible for the age-hardening as well as for the stabilization of grain size. The occurrence of softening is an indication of recrystallization and grain growth as well as the coarsening of precipitate phases.

4.1. Precipitation during isochronal annealing

The Mg-Nd alloy undergoes precipitation during the annealing temperature range of 150–450 °C as used in the present study. A precipitation sequence for a binary supersaturated solid solution (SSS) Mg-Nd alloy was proposed as follows: [34]

SSS → GP zones → β"-Mg_3Nd → β'-Mg_7Nd → β_1-Mg_3Nd → β-$Mg_{12}Nd$ → β_e-$Mg_{41}Nd_5$

The equilibrium β_e-$Mg_{41}Nd_5$ phase was observed only after a very high temperature annealing at 500 °C. [35] The Guinier-Preston (GP) zones, β"-Mg_3Nd and β'-Mg_7Nd phases were reported as formed during the early stage of ageing at low temperatures (150–200 °C). [14] The GP zones and metastable precipitates of the β"-Mg_3Nd and β'-Mg_7Nd phases are responsible for the peak hardening in the Mg–Nd alloy. [36] Nevertheless, those phases were observed only by transmission electron microscopy (TEM), high-angle annular dark field scanning transmission electron microscopy (HAADF-STEM) and atom probe tomography (APT) techniques [14, 34, 36, 37] because of their fine-scale with a size ranging between ~5 and ~15 nm .[36] These small sizes explain the inability to observe these phases in the SEM micrographs from the present investigation as in Figure 3. Furthermore, it is reasonable to anticipate that the sizes of the precipitate phases will be finer in the HPT-deformed sample because of the higher density of nucleation sites. [38]

It is worth noting that the peak hardening was shifted to a low temperature (150 °C) in the present alloy compared to earlier reports for the Mg-Nd alloy (170 °C) and a similar Mg-RE alloy (250 °C). [14, 36, 39] This is attributed to the enhanced diffusivity of Mg and Nd due to the high densities of dislocations and vacancies introduced by the severe plastic deformation. Moreover, it should be noted that the metastable phases such as β'-Mg_7Nd and β_1-Mg_3Nd have a preference for dislocation nucleation. [14, 37, 40] Basically, the presence of dislocations and the excess of vacancies accelerates significantly the kinetics of the precipitation process in the Mg-Nd alloy by acting as heterogeneous nucleation sites and increasing the diffusion rate of solutes. [14, 39–41] Simultaneously, the metastable phases were found to also nucleate around pre-existing particles. [39] Hence, it is expected that the present alloy undergoes a significant amount of precipitation since it was severely deformed by HPT processing and the initial deformed sample contains a reasonable fraction of second phase particles (1.2 ± 0.3%). Thus, the good resistance against a coarsening of grain size when annealing at 150 and 350 °C

is caused by the precipitation of metastable phases and a preferable nucleation at dislocations which prevents boundary movement and annihilation.

Ageing above 250 °C causes a rapid disappearance of GP-zones and the β'-Mg_7Nd phase together with the formation of coarse precipitates of the stable β_1- Mg_3Nd and β - $Mg_{12}Nd$ phases. [36, 42] Furthermore, HPT processing increases the volume fraction of these precipitate phases compared to the non-deformed sample. [27, 41] The average diameter of the β-$Mg_{12}Nd$ phase was reported to increase from ~120 nm to ~300 nm when ageing at 250 and 350 °C, respectively. [39] It is interesting to note that the excess strain-induced vacancies were found to play a significant role in coarsening of the precipitate phases. [42] Based on these observations, the granular precipitates dispersed throughout the microstructure in samples annealed at 350 and 450 °C can be identified as the β-$Mg_{12}Nd$ phase, as denoted by the arrows in Figure 3(h). Close inspection of these microstructures in Figure 3(h) and (j) shows that the diameters of these particles increase with increasing annealing temperature.

In addition, Figure 3(j) shows that after annealing at 450 °C there are some agglomerates of particles in the Mg matrix, shown in the square at lower right, caused probably by the high annealing temperature. Therefore, the disappearance of metastable phases and the coarsening of the stable phases during annealing at 350 °C and 450 °C leads to an overall softening and the strong increase of grain size observed in the present alloy in Figure 2. The thermal stability in annealing at 250C is generally larger as reported in Mg-based alloys after conventional or severe plastic deformation [41, 43–49]. Nevertheless, processing by HPT allows the development of a stable UFG structure with a grain size of ~0.6 μm in the present study or between ~2–5 μm in an Mg-Al-Ca alloy. [43]

4.2 Texture evolution during isochronal annealing

The deformation texture developed in the present Mg-1.43Nd alloy, and as reported earlier in binary Mg-Ce and Mg-Dy alloys where the basal texture was shifted towards SD [28,

[29], was different from that reported for pure Mg where there is a typical basal fiber texture in similar deformation conditions. [50] Such a difference is attributed to the effect of the RE elements in decreasing the stacking fault energy and hence facilitating the activation of <a> prismatic slip and <c+a> pyramidal slip during HPT processing at room temperature. [1, 29] The rearrangement of the <a> prismatic and <c+a> pyramidal slip into a cell structure or sub-grains by cross-slip and climb during the processing operation gives rise to a progressive rotation of the sub-grains from the parent orientation.

It is apparent from Figure 4 that the deformation texture was more or less similar until annealing at 350 °C for 1 h where a split basal texture was produced with peaks along the SD. This texture is similar to the TD-split texture often reported in hot-rolled Mg-RE alloys. [6, 7] Again, annealing at 450 °C gives a different texture with a significant spread along the SD compared to the texture after annealing at 350 °C as in Figure 4(e).

The textures reported in this investigation are different from those reported for the recrystallization textures in Mg-based alloys. Usually, the deformation texture is retained after a recrystallization treatment in Mg-based alloys due the occurrence of dynamic recrystallization during deformation processing. [51–53] As demonstrated in Figure 1(a), the high distorted zones in the microstructure of the HPT-deformed sample reveal the general lack of dynamic recrystallization. Nevertheless, it was reported previously that identical deformation processing and conditions with a Mg-0.44Dy alloy, with processing by HPT at room temperature through 5 turns, led to a homogeneous microstructure with 50% of dynamically recrystallized grains. [29] This difference is attributed to the presence of second phase particles of the $Mg_{12}Nd$ and $Mg_{24}Nd_5$ phases in the Mg-1.43Nd alloy used in the present experiments where these particles restrict the occurrence of dynamic recrystallization. Another factor accounting for the difference between the two Mg-based alloys may be the electronic configuration and chemical differences between the Nd and Dy elements which will affect the deformation and recrystallization mechanisms of both alloys. [13] The results

shown in Figs 2 and 3 indicate that changes in the crystallographic texture during annealing are associated also with the grain size stability.

The recrystallized grains may be identified using the Grain Orientation Spread (GOS) criterion where GOS is defined as the average deviation between the orientation of each point in the grain and the average orientation of the grain. [54] The recrystallized grains were separated from the deformed grains based on the GOS value where recrystallized grains have GOS values less than 1–2°. Figure 6 demonstrates the EBSD maps of deformed and recrystallized grains for the HPT-processed Mg-1.43Nd alloy and after annealing at 250 and 350 °C, respectively.

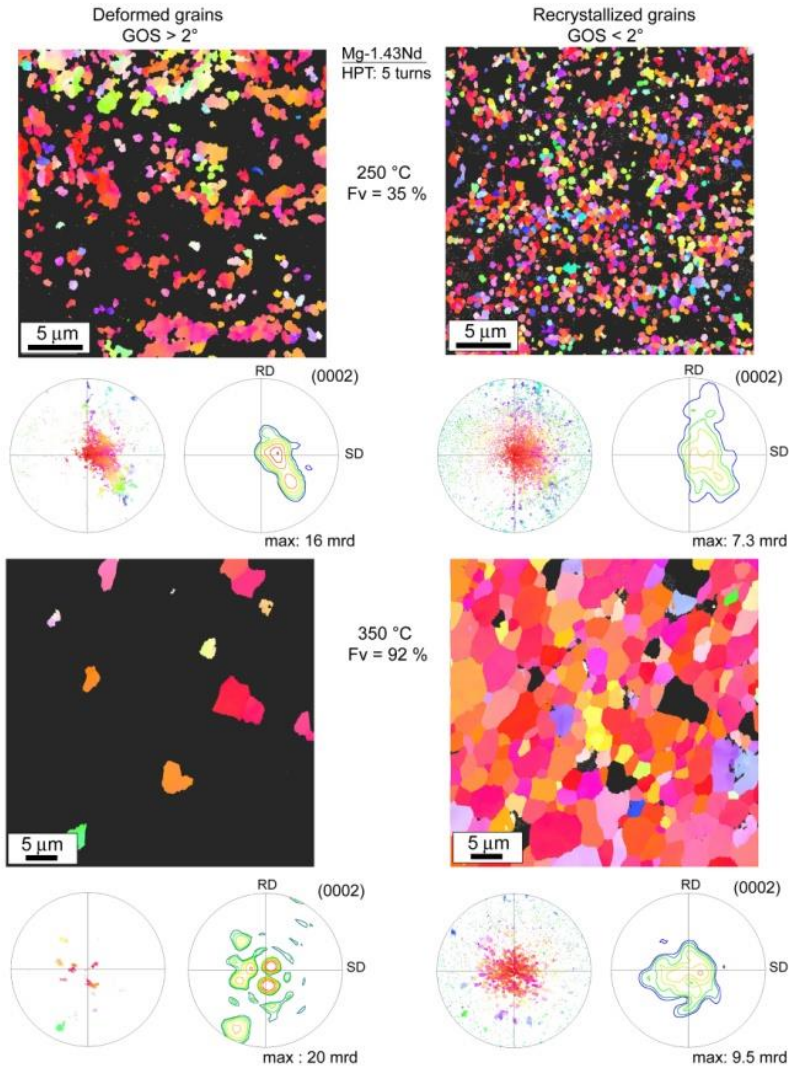

Figure 6: Orientation imaging micrographs and texture data of deformed and recrystallized grains for HPT processed Mg-1.43Nd alloy and annealed at 250 and 350 °C.

The (0002) basal pole figure is also represented in Figure 6, where it is divided in terms of the single orientation scatter and recalculated pole figure of the recrystallized and deformed grains. Thus, the volume fraction of recrystallized grains increases rapidly from 15% to 80 % with increasing annealing temperature. The texture of the recrystallized grains after annealing at 250 °C is significantly scattered and obviously deviates from the deformed grains. However, it is also observed that the deformed grains remaining after annealing at 350 °C have different orientations from the recrystallized grains.

From these analyses, it is concluded that the preferred growth of recrystallized grains with deformed orientations after annealing at 250 °C leads probably to the nucleation of metastable phases that delay recrystallization and prevent any growth related to a texture modification. In addition, the pinning effect of precipitation is suppressed during annealing at 350 °C which permits the development of new recrystallized grains with different textures by oriented nucleation events which are most probably governed by nucleation at shear bands. [55]

Annealing at the relatively high temperature of 450 °C causes a more angular spread of basal poles along RD and SD as a consequence of the extensive increase in grain size due the additional thermal activation and more rapid growth rate. The presence of extension twins in the microstructure of the annealed sample, as in Figure 1(e), also adds to the change in the texture. Finally, the occurrence of twins introduces high misorientation angles between the grains and the twinning and this also significantly changes the final texture. [56]

4.3. Hall-Petch relationship

The Hall–Petch relationship for the isochronally annealed Mg-1.43Nd alloy was used in order to examine the contribution of any grain boundary strengthening mechanism in the evolution of microhardness. The microhardness data from Figure 5 were re-plotted against $d^{-1/2}$ in Figure 7 following the relationship: [57]

$$H_v = H_{v0} + K_H d^{-1/2} \quad (1)$$

where H_v is the measured hardness, H_{v0} is the friction hardness which represents the resistance of the crystal lattice to the movement of dislocation and K_H is a locking parameter which indicates the contribution of the grain boundaries to the hardening. [58] These parameters may be calculated directly from a linear fit to the curve in Figure 7. Thus, the fitted constants from Figure 7 are: H_{v0} = 38.6 and K_H = 42.9 $\mu m^{1/2}$.

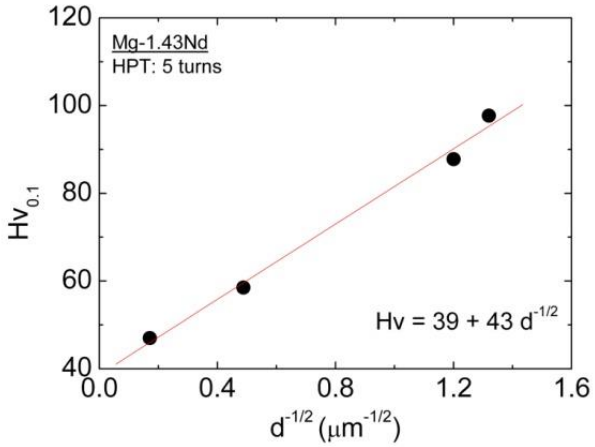

Figure 7: Microhardness plotted against mean grain size representing the Hall–Petch relationship for Mg-1.43Nd alloy processed by HPT through 5 turns and subsequent annealing.

It is interesting to note that this value of H_{v0} is close to the microhardness value of the as-cast Mg-1.43Nd alloy (44 ± 3 Hv). Similar values were also documented (H_{v0} = 38, K_H = 42) in an AZ31 alloy processed by ECAP [59] and it was reported that reinforcing AZ31 alloy with Al_2O_3 nano-particles increased both the values of the friction hardness and the locking parameter (H_{v0} = 38.8, K_H = 60.9) compared to the conventional AZ31alloy (H_{v0} =36.7, K_H = 51.7). [58] Accordingly, the similar values found in the present binary alloy compared to the industrial ternary AZ31 alloy is attributed to the grain boundary strengthening from the pinning mechanism introduced by the precipitate particles and by their role in restricting dislocation movement during deformation induced by the penetration of the microhardness indenter.

4.4. Grain growth kinetics

The grain growth rate, X, may be determined using the conventional Arrhenius equation: [60]

$$X = Aexp\left(-\frac{Q}{RT}\right) \quad (2)$$

where A is the pre-exponential constant, R is the gas constant, Q is the activation energy for grain growth and T is the absolute annealing temperature. The grain growth rate may be expressed as a function of the mean grain size so that: [60]

$$X = \frac{d^n - d_0^n}{t} \quad (3)$$

where d is the grain size after annealing, d_o is the grain size before annealing, t is the time for annealing where t = 1 h in these experiments and n is the grain growth exponent. Usually, the value of n is in the range from 2 to 4 for Mg alloys processed by SPD [61] and therefore the value was taken as equal to 2 in the present study.

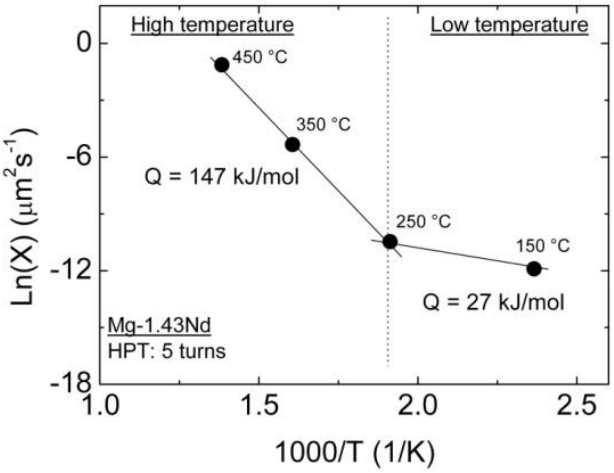

Figure 8: Evolution of ln*(X)* as a function of 1000/*T* (K^{-1}) for Mg-1.43Nd alloy processed by HPT through 5 turns and subsequent annealing.

Figure 8 presents the evolution of ln*(X)* as a function of 1000/*T*(K^{-1}) for Mg-1.43Nd processed by HPT through 5 turns and with subsequent annealing up to 450 °C for 1 h. It is clear that two temperature ranges having different activation energies may be identified from this plot. The activation energy, Q, calculated from the slopes of the experimental data in the

low temperature range of 150–250 °C is equal to ~26 kJ/mol and in the high temperature range of 250–450 °C it is equal to ~147 kJ/mol. The activation energy in the low temperature range is much lower than the anticipated value for boundary self-diffusion in pure Mg (~92 kJ mol^{-1}) [62] and, moreover, it is expected that the activation energy of grain boundary diffusion will be higher in alloys than in pure metals. [58] In the high temperature range, the value of *Q* is very similar to the value for lattice self-diffusion in pure Mg (~135 kJ mol^{-1}) [62] and the small difference may be caused by the presence of second phase particles. [63] Thus, it is concluded that lattice self-diffusion is the dominant mechanism for grain growth in the severely deformed Mg-1.43Nd alloy in the high temperature range. This is in good agreement with the assumption that lattice self-diffusion is the dominant process of grain growth when the alloy consists of large grains [64] which is correct for the present alloy after annealing at 350 and 450 °C. In fact, a strong basal texture was reported as also responsible for an increase in the activation energy for grain growth [65] and, as can be seen from Figure 4, the texture of the present alloy starts to change after annealing at 250 °C where a basal texture is well developed.

It appears that the activation energy in the low temperature range corresponds to the energy needed for the recovery and recrystallization of ultrafine grains, as demonstrated by the stabilization of the mean grain size between the deformed state and annealing at 250 °C as shown in Figure 2. Furthermore, the energy in the high temperature range is required for grain growth from a fine recrystallized microstructure to a coarse structure, as is evident from the increase in the mean grain size from ~0.65 μm after annealing at 250 °C to ~34 μm after annealing at 450 °C.

There are several investigations reporting similar low activation energies for grain growth (~19–50 kJ/mol) in Mg-based alloys. [58, 59, 66–68] For example, an activation energy of 24.5 kJ/mol was obtained in the temperature range of 250–400 °C in AZ31 processed by ECAP at 200 °C though 4 passes using route Bc and then annealing for 30 min. [59] An

exceptionally low activation energy of 19.2 kJ/mol was reported in the temperature range of 257–427 °C for AZ31 reinforced with Al_2O_3 nano-particles after ECAP processing at 227 °C for 4 passes using route Bc and then annealing for 30 min. [58] Additionally, the activation energy of a hot extruded Mg-Gd-Y-Zr alloy was reported as ~50 kJ/mol in the relatively high temperature range of 400–450 °C. [66] Detailed examination shows that the temperature range of the low activation energy in the present study is much lower (150–250 °C) than in these earlier reports (~200–400°C). [58, 59, 66] This difference may be associated with the different types of processing (HPT vs. ECAP) and the different deformation temperatures (room temperature vs. hot deformation) which will significantly affect the mean grain size and thus the grain growth process. It is well known that HPT processing has the capability of causing greater microstructural instability because of the inherent high dislocation density and/or the high concentration of vacancies compared to other SPD processing procedures such as ECAP. [69] It was demonstrated earlier that processing by HPT can lower the recrystallization temperature and lead to a decrease in the stored energy with increasing HPT turns in Mg-RE alloys. [26]

Two main hypotheses were proposed to provide an explanation of this very low activation energy. The first hypothesis was that grain growth under unrecrystallized conditions, caused by the presence of a high extrinsic dislocation density in the non-equilibrium grain boundaries, may lead to a higher atomic mobility compared to conventional equilibrium grain boundaries. [58, 70] Vacancies are needed for the climb of dislocations and therefore these extra vacancies will assist the climb process and this will tend to enhance the recrystallization. This is in good agreement with the assumption that SPD processing may decrease the activation energy of grain boundary diffusion in UFG alloys. [71, 72] The second hypothesis was that grain growth under recrystallized conditions may lead to a low activation energy due to a progressive decrease in the dislocation density through enhanced recovery with an increase in the annealing temperature. [59, 67] A consideration of these alternatives

suggests that the first hypothesis is more appropriate to explain the low activation energy in the present study since no recrystallized grains were observed within the deformed microstructure as in Figure 1(a). Another factor is the presence of precipitate particles during annealing. These particles act as obstacle to the movement of dislocations and delay their annihilation which will cause a reduction in the internal energy [73] and, in addition, a part of this stored energy will be consumed by the growth of the precipitates during annealing.

5. Conclusions

1. The thermal stability of an Mg-1.43Nd alloy was investigated using EBSD and Vickers microhardness measurements after processing by HPT trough 5 turns and subjecting to isochronal annealing at temperatures ranging from 150–450 °C.

2. The HPT-processed alloy exhibits good thermal stability at lower temperatures. Processing through 5 turns produces significant grain refinement with an average grain size of ~0.6 μm. This mean grain size remains stable on annealing up to 250 °C but there is major grain growth to ~34 μm after annealing at 450 °C.

3. HPT processing produces a basal texture inclined by 60° from RD towards SD. This texture is retained after annealing at 150 and 250 °C but a TD-split texture develops starting from annealing at 350 °C.

4. The microhardness shows an initial hardening after annealing at 150 °C due precipitation and then a subsequent softening caused by recrystallization and grain growth phenomena. HPT processing decreases the optimum ageing condition (150 °C) compared to the conventional treatment in Mg-based alloys.

5. The kinetics of grain growth in this alloy follows two stages depending on the temperature annealing range. Activation energies of ~26 and ~147 kJ/mol were measured in the low temperature range (150–250 °C) and the high temperature range (250–450 °C), respectively. At low temperatures the grain growth is controlled by the higher mobility of the

non-equilibrium grain boundaries in the deformed ultrafine-grained microstructure whereas at high temperatures the grain growth is governed by lattice self-diffusion.

6. *Acknowledgements*

HA gratefully acknowledges Dr. Talal Al-Samman, Institut für Metallkunde und Metallphysik (IMM-RWTH), Aachen, Germany, for supplying the Mg-RE alloys. YH and TGL were supported by the European Research Council under ERC Grant Agreement No. 267464-SPDMETALS.

Received: ((will be filled in by the editorial staff))
Revised: ((will be filled in by the editorial staff))
Published online: ((will be filled in by the editorial staff))

References

[1] A. Imandoust, C.D. Barrett, T. Al-Samman, K.A. Inal, H. El Kadiri, *J. Mater. Sci.* **2017**, *52*, 1.

[2] S. You, Y. Huang, K.U. Kainer, N. Hort, *J. Magnes. Alloy.* **2017**, *5*, 239.

[3] L.W.F. Mackenzie, F.J. Humphreys, G.W. Lorimer, K. Savage, T. Wilks. in *Magnesium Alloys and Their Applications*, (Eds. K.U. Kainer) , DGM, Germany, **2003**, p. 158.

[4] N. Stanford, M.R. Barnett, *Mater. Sci. Eng. A* 2008, *496*, 399.

[5] N. Stanford, D. Atwell, M.R. Barnett, *Acta Mater.* **2010**, *58*, 6773.

[6] T. Al-Samman, X. Li, *Mater. Sci. Eng. A* **2011**, *528*, 3809.

[7] H. Azzeddine, D. Bradai, *Mater. Sci. Forum* **2012**, *702-703*, 453.

[8] E.A. Ball, P.B. Prangnell, *Scr. Metall. Mater.* **1994**, *31*, 111.

[9] H. Yan, S. Xu, R. Chen, S. Kamado, T. Honma, E. Han. Twins, *Scr. Mater.* **2011**, *64*, 141.

[10] K. Hantzsche, J. Bohlen, J. Wendt, K.U. Kainer, S.B. Yi, D. Letzig, *Scr. Mater.* **2010**, *63*, 725.

[11] S. Sandlobes, S. Zaefferer, I. Schestakow, S. Yi, R. Gonzalez-Martinez, *Acta Mater.* **2011**, *59*, 429.

[12] C.D. Barrett, H. El Kadiri, *Acta Mater.* **2014**, *63*, 1.

[13]. L.L. Rokhlin in *Magnesium alloys containing rare earth metals: Structure and Properties*, Taylor & Francis, New York, **2003**.

[14] D. Choudhuri, N. Dendge, S.N.S. Meher, T. Alam, M.A. Gibson, R. Banerjee, *J. Mater. Sci.* **2014**, *49*, 6986.

[15] B.L. Wu, Y.H. Zhao, X.H. Du, Y.D. Zhang, F. Wangner, C. Esling, *Mater. Sci. Eng. A* **2010**, *527,* 4334.

[16] X. Li, T. Al-Samman, G. Gottstein, *Mater. Lett.* **2011**, *65,* 1907.

[17] X. Hou, Q. Peng, Z. Cao, S. Xu, S. Kamado, L. Wang L, Y. Wu, L. Wang, *Mater. Sci. Eng. A* **2009**, *520,* 162.

[18] C.L.P. Silva, R.B. Soares, P.H.R. Pereira, R.B. Figueiredo, V.F.C. Lins, T.G. Langdon, *Adv. Eng. Mater.* **2019**, *21,* 1801081.

[19] R. Alizadeh, R. Mahmudi, A.H.W. Ngan, Y. Huang, T.G. Langdon, *Mater. Sci. Eng. A* **2016**, *651,* 786.

[20] R. Alizadeh, R. Mahmudi, P.H.R. Pereira, Y. Huang, T.G. Langdon, *Mater. Sci. Eng. A* **2017**, *682,* 577.

[21] M.M. Castro, P.H.R. Pereira, A. Isaac, R.B. Figueiredo, T.G. Langdon, *J. Alloys Compd.* **2019**, *780,* 422.

[22] J. Cizek, I. Prochazka, B. Smola, I. Stulíkova, R. Kuzel, Z. Matej, V. Cherkaska, R.K. Islamgaliev, O. Kulyasova, *Mater. Sci. Eng. A* **2007**, *462,* 121.

[23] Y. Huang, R.B. Figueiredo, T. Baudin, A.L. Helbert, F. Brisset, T.G. Langdon, *J. Mater. Sci.* **2012**, *47,* 7796.

[24] M. Kai, Z. Horita, T.G. Langdon, *Mater. Sci. Eng. A* **2008**, *488,* 117.

[25] R.B. Figueiredo, T.G. Langdon, *Adv. Eng. Mater.* **2019**, *21,* 1801039.

[26] Y.I. Bourezg, H. Azzeddine, Y. Huang, D. Bradai, T.G. Langdon, in Proc. 26th International Conference on Metallurgy and Materials, Burno, **2016**, 1524.

[27] Y.I. Bourezg, H. Azzeddine, L. Hennet, D. Thiaudière, Y. Huang, D. Bradai, T.G. Langdon, *J. Alloys Compd.* **2017**, *719,* 236.

[28] Y.I. Bourezg, H. Azzeddine, T. Baudin, A-L Helbert, Y. Huang, D. Bradai, T.G. Langdon, *Mater. Sci. Eng. A* **2018**, *724,* 477.

[29] A. Hanna, H. Azzeddine, R. Lachhab, T. Baudin, A.L. Helbert, F. Brisset, Y. Huang, D. Bradai, T.G. Langdon, *J. Alloys Compd.* **2019**, *778,* 61.

[30] A. Hanna, H. Azzeddine, Y. Huang, D. Bradai, J.M. Cabrera, T. G. Langdon, *Mater. Charact.* **2019**, *151,* 519.

[31] R.B. Figueiredo, P.R. Cetlin, T.G. Langdon, *Mater. Sci. Eng. A* **2011**, *528,* 8198.

[32] R. Hielscher, H. Schaeben, *J. Appl. Cryst.* **2008**, *41,* 1024.

[33] J. Yan, Y. Sun, F. Xue, S. Xue, W. Tao, *Mater. Sci. Eng. A* **2008**, *476,* 366.

[34] A.R. Natarajan, E.L.S. Solomon, B. Puchala, E.A. Marquis, A. Van der Ven, *Acta Mater.* **2016**, *108,* 367.

[35] M.A. Easton, M.A. Gibson, D. Qiu, S.M. Zhu, J. Grobner, R. SchmidFetzer, J.R. Nie, M.X. Zhang, *Acta Mater.* **2012**, *60*, 4420.

[36] K. Saito, K. Hiraga, *Mater. Trans.* **2011**, *52*, 1860.

[37] Y.M. Zhu, H. Liu, Z. Xu, Y. Wang, J.F. Nie, *Acta Mater.* **2015**, *83*, 239.

[38] O. Melikhova, J. Čížek, P. Hruška, M. Vlček, I. Procházka, M. Vlach, I. Stulíková, B. Smola, N. Žaludová, R. K. Islamgaliev, *Defect and Diffusion Forum* **2012**, *322*, 151.

[39] L.Y. Wei, G.L. Dunlop, H. Westengen, *J. Mater. Sci.* **1996**, *31*, 387.

[40] T.J. Pike, B. Noble, *J. Less-Common Met.* **1973**, *30*, 63.

[41] S.V. Dobatkin, L.L. Rokhlin, E.A. Lukyanova, M.Y. Murashkin, T.V. Dobatkina, N. Y. Tabachkov, *Mater. Sci. Eng. A* **2016**, *667*, 217.

[42] L. Couturier, A. Deschamps, F. De Geuser, F. Fazeli, W.J. Poole, *Scripta Mater.* **2017**, *136*, 120.

[43] S.V. Dobatkin, Y. Estrin, L.L. Rokhlin, M.V. Popov, R. Lapovok, T. V. Dobatkina, V.N. Timofeev, N.I. Nikitina, *Mater. Sci. Forum* **2008**, *584-586*, 559.

[44] H.Y. Chao, H.F. Sun, W.Z. Chen, E.D. Wang, *Mater. Charact.* **2011**, *62*, 312.

[45] J. Su, M. Sanjari, A. H. Kabir, J.J. Jonas, S. Yue, *Mater. Sci. Eng. A* **2016**, *662*, 412.

[46] J.P. Young, H. Askari, Y. Hovanski, M.J. Heiden, D.P. Field, *Mater. Charact.* **2015**, *101*, 9.

[47] S.K. Mishra, S.M. Tiwari, J.T. Carter, A. Tewari, *Mater. Sci. Eng. A* **2014**, *599*, 1.

[48] L. Tang, Y. Zhao, R.K. Islamgaliev, R.Z. Valiev, Y.T. Zhu, *J. Alloys Compd.* **2017**, *721*, 577.

[49] H.K. Lin, J.C. Huang, T.G. Langdon, *Mater. Sci. Eng. A* **2005**, *402*, 250.

[50] D. Ahmadkhaniha, Y. Huang, M. Jaskari, A. Järvenpää, M. H. Sohi, C. Zanella, L. P. Karjalainen, T. G. Langdon, *J. Mater. Sci.* **2018**, *53*, 16585.

[51] H. Azzeddine, D. Bradai, *Int. J. Mater. Res.* **2012**, *11*, 1351.

[52] S. Abdessameud, H. Azzeddine, B. Alili, D. Bradai, *Trans. Nonferrous Met. Soc. China* **2010**, *20*, 2215.

[53] T. Al-Samman, G. Gottstein, *Mater. Sci. Eng. A* **2008**, *490*, 411.

[54] J.H. Cho, A. Rollett, K. Oh, *Metall. Mater. Trans.* **2005**, *36*, 3427.

[55] I. Basu, T. Al-Samman, G. Gottstein, *Mater. Sci. Eng. A* **2013**, *579*, 50.

[56] I. Basu, T. Al-Samman, *Mater. Sci. Eng. A* **2017**, *707*, 232.

[57] R. Armstrong, *Acta Mech.* **2014**, *225*, 1013.

[58] Y. Radi, R. Mahmudi, *Mater. Sci. Eng. A* **2010**, *527*, 2764.

[59] H.K. Kim, W.J. Kim, *Mater. Sci. Eng. A* **2004**, *385*, 300.

[60] J.E. Burke, D. Turnbull, *Prog. Metal Phys.* **1952**, *3,* 220.

[61] Q. Miao, L. Hu, X. Wang, E. Wang, *J. Alloy Compd.* **2010**, *493,* 87.

[62] H.J. Frost, M.F. Ashby in *Deformation Mechanism Maps: The Plasticity and Creep of Metals and Ceramics*, Oxford: Pergamon Press, U.K, **1982**.

[63] O. Lambri, W. Riehemann, Z. Trojanova, *Scr. Mater.* **2001**, *45,* 1365.

[64] J. Straska, J. Strasky, M. Janecek, *Acta Phys. Pol. A* **2015**, *128,* 578.

[65] J. Ma, X. Yang, Q. Huo, H. Sun, J. Qin, J. Wang, *Mater. Des.* **2013**, *47,* 505.

[66] R. Alizadeh, R. Mahmudi, A. H. W. Ngan, T. G. Langdon, *J. Mater. Sci.* **2015**, *50,* 4940.

[67] H.K. Kim, *J. Mater. Sci.* **2004**, *29,* 7107.

[68] G.H. Huang, D.D. Yin, J.W. Lu, H. Zhou, Y. Zeng, G.F. Quan, Q.D. Wang, *Mater. Sci. Eng. A* **2018**, *720,* 24.

[69] A.P. Zhilyaev, T.G. Langdon, *Prog. Mater. Sci.* **2008**, *53,* 893.

[70] J. Wang, Y. Iwahashi, Z. Horita, M. Furukawa, M. Nemoto, R.Z. Valiev, T.G. Langdon, *Acta Mater.* **1996**, *44,* 2973.

[71] R.Z. Valiev, E.V. Kozlov, Y.F. Ivanov, J. Lian, A.A. Nazarov, B. Baudelet, *Acta Metall.* **1994**, *42,* 2467.

[72] J. Lian, R.Z. Valiev, B. Baudelet, *Acta Metall.* **1995**, *43,* 44165.

[73] A. Dhal, S.K. Panigrahi, M.S. Shunmugam, *J. Alloys Compd.* **2015**, *649,* 229.